


## Extended phase diagram of $La_{1-x}Ca_xMnO_3$ by interfacial engineering

Kexuan Zhang(张可璇), Lili Qu(屈莉莉), Feng Jin(金锋), Guanyin Gao(高关胤), Enda Hua(华恩达), Zixun Zhang(张子璔), Lingfei Wang(王凌飞), and Wenbin Wu(吴文彬)

**Citation:**Chin. Phys. B, 2021, 30 (**12**): 126802. DOI: 10.1088/1674-1056/ac003e
Journal homepage: http://cpb.iphy.ac.cn; http://iopscience.iop.org/cpb

**What follows is a list of articles you may be interested in**

---

## Light-matter interaction of 2D materials: Physics and device applications

Zi-Wei Li(李梓维), Yi-Han Hu(胡义涵), Yu Li(李瑜), Zhe-Yu Fang(方哲宇)
Chin. Phys. B, 2017, 26 (**3**): 036802. DOI: 10.1088/1674-1056/26/3/036802

## Interface effect on structural and electronic properties of graphdiyne adsorbed on $SiO_2$ and h-BN substrates: A first-principles study

Dong Bao-Juan, Yang Teng, Wang Ji-Zhang, Zhang Zhi-Dong
Chin. Phys. B, 2015, 24 (**9**): 096806. DOI: 10.1088/1674-1056/24/9/096806

## Adsorptions and diffusions of carbon atoms on the surface and in the subsurface of Co (200)： A first-principles density-functional study

Qiao Liang, Wang Shu-Min, Zhang Xiao-Ming, Hu Xiao-Ying, Zeng Yi, Zheng Wei-Tao
Chin. Phys. B, 2014, 23 (**8**): 086802. DOI: 10.1088/1674-1056/23/8/086802

## Resonant energy transfer from nanocrystal Si to β-$FeSi_2$ in hybrid Si/β-$FeSi_2$ film

He Jiu-Yang, Zhang Qi-Zhen, Wu Xing-Long, Chu Paul K.
Chin. Phys. B, 2013, 22 (**10**): 106804. DOI: 10.1088/1674-1056/22/10/106804

## Methane adsorption on graphite(0001) films: a first-principles study

He Man-Chao, Zhao Jian
Chin. Phys. B, 2013, 22 (**1**): 016802. DOI: 10.1088/1674-1056/22/1/016802

---

RAPID COMMUNICATION

# Extended phase diagram of $La_{1-x}Ca_xMnO_3$ by interfacial engineering*

Kexuan Zhang(张可璇)[1], Lili Qu(屈莉莉)[1], Feng Jin(金锋)[1], Guanyin Gao(高关胤)[1], Enda Hua(华恩达)[1], Zixun Zhang(张子璔)[1], Lingfei Wang(王凌飞)[1,†], and Wenbin Wu(吴文彬)[1,2,‡]

[1] *Hefei National Laboratory for Physical Sciences at Microscale, University of Science and Technology of China, Hefei* 230026, *China*
[2] *Anhui Key Laboratory of Condensed Matter Physics at Extreme Conditions, High Magnetic Field Laboratory, HFIPS, Anhui, Chinese Academy of Sciences, Hefei* 230031, *China*

(Received 2 April 2021; revised manuscript received 5 May 2021; accepted manuscript online 12 May 2021)

The interfacial enhanced ferromagnetism in maganite/ruthenate system is regarded as a promising path to broaden the potential of oxide-based electronic device applications. Here, we systematically studied the physical properties of $La_{1-x}Ca_xMnO_3/SrRuO_3$ superlattices and compared them with the $La_{1-x}Ca_xMnO_3$ thin films and bulk compounds. The $La_{1-x}Ca_xMnO_3/SrRuO_3$ superlattices exhibit significant enhancement of Curie temperature ($T_C$) beyond the corresponding thin films and bulks. Based on these results, we constructed an extended phase diagram of $La_{1-x}Ca_xMnO_3$ under interfacial engineering. We considered the interfacial charge transfer and structural proximity effects as the origin of the interface-induced high $T_C$. The structural characterizations revealed a pronounced increase of B–O–B bond angle, which could be the main driving force for the high $T_C$ in the superlattices. Our work inspires a deeper understanding of the collective effects of interfacial charge transfer and structural proximity on the physical properties of oxide heterostructures.

**Keywords:** interfacial engineering, oxygen octahedral coupling, charge transfer, oxide superlattices

**PACS:** 68.35.Rh, 68.65.Cd, 75.30.Et, 75.25.Dk **DOI:** 10.1088/1674-1056/ac003e

## 1. Introduction

At the $ABO_3$ perovskite oxide interfaces, the charge, orbital, spin, and lattice degrees of freedom are strongly coupled.[1] Hence, interfacial engineering holds great potential for exploiting intriguing physical phenomena and controllable functionalities in $ABO_3$ perovskite oxides.[2] The interfacial structural proximity effect and charge reconstruction are two essential routes to tune the physical properties of oxide heterostructures.[3] On the one hand, the universally required connectivity of $BO_6$ octahedra enables the coherence of octahedral distortion (tilting, rotation, and deformation) across the heterointerface,[4] leading to the so-called interfacial oxygen octahedral coupling (OOC).[5] On the other hand, charge transfer across the oxide interface can be triggered by polar discontinuity, differences in valence states, or different electro-negativity.[6–8] Both the interfacial OOC and charge transfer can lead to pronounced modulations of magnetic and electrical properties.[6,8,9]

The maganite/ruthenate heterostructures have attracted intensive research attention due to the abundant interfacial properties.[10–12] The ferromagnetic order in ultrathin $La_{0.67}Ca_{0.33}MnO_3$ layers is found to be stabilized when interfaced with nonmagnetic $CaRu_{1-x}Ti_xO_3$ (CRTO) and the ferromagnetic $SrRuO_3$ (SRO).[13–16] How does the ruthenate/manganite interface affect the phase diagram of $La_{1-x}Ca_xMnO_3$ [LCMO($x$)] is still an open question. The hole-doped $La_{1-x}Ca_xMnO_3$ [LCMO($x$)] ($0 < x < 0.5$) is a typical mixed-valence manganite, which exhibits a complex phase diagram with diverse magnetic and electronic ground states, such as paramagnetic (PM) insulator, ferromagnetic insulator (FI), ferromagnetic metal (FM), canted antiferromagnet (CAF), charge-ordered antiferromagnet (CO-AF), etc.[17,18] It has been well accepted that the Zener's double exchange (DE) interaction between $Mn^{3+}$ and $Mn^{4+}$ is essential to dertermine the magnetic order and conductivity of maganites.[17,19] Both the chemical valence of Mn ions and the structural distortions of $MnO_6$ octahedra can modify the electron transfer underlying the DE interaction, therefore regulate the magnetic and electrical properties of maganites.[20,21] Accordingly, the superlattices (SLs) composed of LCMO($x$) and SRO layers, where the cooperative charge transfer and OOC are expected, could be a feasible way to extend the phase diagram of LCMO($x$).

In this work, we systematically investigated the interfacial-mediated enhancement of ferromagnetism in

*Project supported by the National Key Research and Development Program of China (Grant Nos. 2016YFA0401003, 2017YFA0403502, and 2020YFA0309100), the National Natural Science Foundation of China (Grant Nos. 11974326, 12074365, 11804342, U2032218, and 51872278), the Fundamental Research Funds for the Central Universities, China (Grant Nos. WK2030000035 and WK2340000102), and Hefei Science Center of Chinese Academy of Sciences (Grant No. 2020HSC-UE014).

†Corresponding author. E-mail: wanglf@ustc.edu.cn
‡Corresponding author. E-mail: wuwb@ustc.edu.cn

© 2021 Chinese Physical Society and IOP Publishing Ltd 

LCMO($x$) system with various Ca doping levels ranging from 0.005 to 0.429. We compared the physical properties of 35 nm-thick LCMO($x$) single-phase films and [LCMO($x$) (2.4 nm)/SRO (1.2 nm)]$_{10}$ superlattices (SLs), denoted as LCMO($x$)/SRO SLs. The LCMO($x$)/SRO SLs exhibit higher Curie temperature ($T_C$) than the corresponding LCMO($x$) thin films and bulk compounds in a wide doping range, indicating a robust enhancement of ferromagnetism by interfacial effects. We first qualitatively discussed the interfacial charge transfer at the LCMO($x$)/SRO heterointerface and concluded that it is not the main reason for the enhanced ferromagnetism. Then we investigated the structural proximity effect in the LCMO($x$)/SRO SLs and found that the octahedral tilt is largely suppressed in the LCMO($x$)/SRO SLs. We suggest that the enlarged B–O–B bond angles can widen the bandwidth of $e_g$ electrons, therefore enhance the double exchange interaction and ferromagnetism in ultrathin LCMO($x$) layers. Our findings and investigations are likely to extend the magnetic properties of epitaxial LCMO($x$) ultrathin films for spintronic devices.

## 2. Methods and material

The ceramic targets of LCMO($x$) and SRO were prepared by traditional solid-state reactions, with altering Ca fraction ($x$) of 0.005, 0.125, 0.200, 0.250, 0.333, and 0.429. The original compounds, i.e., $La_2O_3$, CaO, $MnO_2$, $RuO_2$, and $SrCO_3$ powder were mixed according to the stoichiometry and then reacted at 1050 °C, 1150 °C, and 1250 °C for 12 hours, respectively. After pressing into ∼ 20 mm diameter disk at 30 MPa, the targets were sintered at 1350 °C for 24 hours.

The proposed samples in this article are epitaxial LCMO($x$) single layers (35 nm) and LCMO($x$)/SRO SLs epitaxially grown on 001-oriented $NdGaO_3$ (NGO) substrates via pulsed laser deposition (PLD) method. In the SLs, the thickness of LCMO($x$) and SRO layers is fixed to 2.4 nm (∼ 6 u.c.) and 1.2 nm (∼ 3 u.c.). The LCMO($x$)/SRO bilayers were repeatedly grown by 10 times. An additional SRO layer was deposited on the top of the SL to ensure that every LCMO($x$) layer has the same structural and magnetic boundary conditions. During deposition, the substrate temperature was set to be 730 °C and the oxygen pressure was kept at 35 Pa. Thickness of each layer in the SLs was fixed by controlling the depositing time.

Structural characterizations of the samples were carried out by x-ray diffraction (XRD) measurements, including $\omega$–$2\theta$ linear scans and reciprocal space mappings (RSMs). Magnetic properties were measured by a vibrating sample magnetometer (Quantum Design, VSM). The resistivity measurements were performed with a standard four-probe method on a physical property measurement system (Quantum Design, PPMS). During the magnetic and resistivity measurements, the magnetic field was applied along the orthorhombic [010] direction, which is the in-plane easy-axis of the LCMO($x$)/SRO SLs.

## 3. Results and discussion

LCMO($x$), SRO, and NGO have the same orthorhombic *Pbnm* symmetry but distinct octahedral rotation and tilt angles. As schematically shown in Fig. 1, the corner-sharing $BO_6$ octahedra in the orthorhombic *Pbnm* structure have $a^-a^-c^+$ tilt and rotation pattern. The $RuO_6$ and $GaO_6$ octahedra are nearly regular and rigid, while the $MnO_6$ octahedra are slightly deformed by the Jahn–Teller distortion. Owing to the structural constraint from the strain effect, the in-plane parameters of the coherently grown LCMO($x$) films and LCMO($x$)/SRO SLs keep consistent with the NGO (001) substrate. Meanwhile, the tilt and rotation angle of $MnO_6$ and $RuO_6$ in the epitaxial samples is supposed to deviate from the bulk due to the interfacial OOC, which is essential for the physical properties and will be studied below.

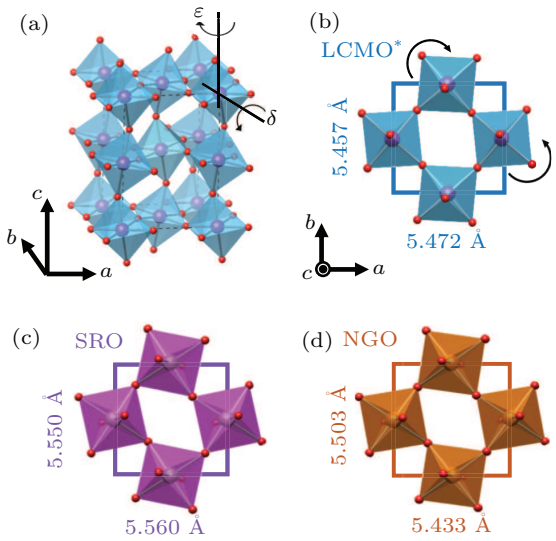



**Fig. 1.** Schematic of the orthorhombic *Pbnm* structure of perovskite oxides with $a^-a^-c^+$ tilt/rotation pattern. The $BO_6$ octahedra are corner-shared across the heterointerfaces in the SLs. (a) The perspective view of a unit cell of LCMO(0.333). The octahedra tilt ($\delta$) and rotation ($\varepsilon$) are schematically shown with solid arrows. (b)–(d) The view along the [001] direction of LCMO, SRO, and NGO, respectively. The lattice parameters shown in (b) represent the composition of LCMO(0.333).

The epitaxial quality of the samples was checked by XRD $\omega$–$2\theta$ linear scans. Figure 2 shows the XRD curves measured from the LCMO($x$) single layers [Fig. 2(a)] and LCMO/SRO SLs [Fig. 2(b)] near NGO (004) reflections. Clear Laue fringes can be observed for all the scans, indicating the high crystal quality and sharp interfaces of the epitaxial samples. The positions of (004) diffractions shift to higher angle as Ca doping level $x$ increases, implying a reduction of lattice constant $c$, which can be attributed to the reduction of averaged $A$-site cation radius.

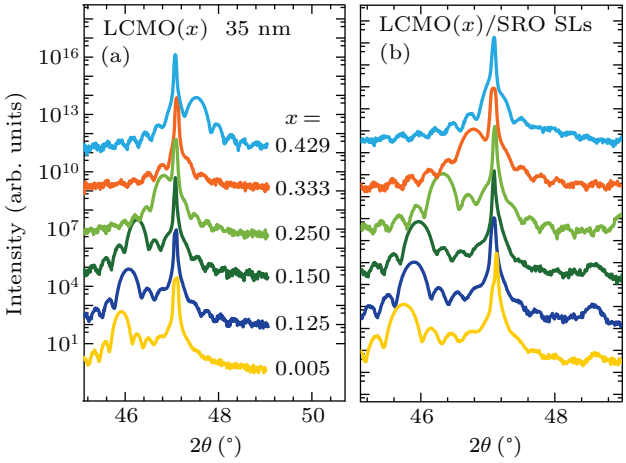



**Fig. 2.** XRD linear scans ($\omega$–$2\theta$) near NGO (004) reflections. (a) XRD curves of 35 nm-thick LCMO($x$) single layers. (b) XRD curves of [LCMO($x$) (2.4 nm)/SRO (1.2 nm)]$_{10}$ SLs.

After clarifying the structural evolutions, we turn to characterize the magnetic and electrical properties of LCMO($x$) single layers. The temperature-dependent magnetization ($M$–$T$) and resistivity ($\rho$–$T$) are shown in Figs. 3(a) and 3(b), respectively. The strong PM signal from the NGO substrate has been subtracted from the $M$–$T$ curves. According to the magnetic and conducting behavior of the LCMO($x$) films, we classify them into three sorts. First, pronounced ferromagnetic transition at 185 K, 218 K, and 254 K can be observed in LCMO films with $x = 0.200$, 0.250, and 0.333, respectively. These ferromagnetic transitions are accompanied by metal-to-insulator transitions (MIT) at the same $T_C$. As $T$ decreases below $T_C$, the magnetization in these three films first increases and then saturates, implying that all these films have a FM ground state, consistent with the corresponding bulk compounds. Second, the light-doped LCMO film with $x = 0.005$ (0.125) shows a clear $T_C$ at 142 K (139 K), and a drop of $M$ at 84 K (69 K). The $\rho$–$T$ curves exhibit insulating behavior. Therefore, we suggest that the LCMO films with $x = 0.005$ and 0.125 show first a FI transition and then a CO-AF ground state. This behavior is similar to that of bulk LCMO with $x = 0.125$.[22,23] Note that the LCMO(0.005) film presents a similar phase transition with LCMO(0.125), instead of the CAF ground state observed in the LCMO(0.005) bulk. Previous works have predicted that the CAF state is induced by the competition between super-exchange (SE) and DE interactions, which is unstable against phase separation into FM and AFM states in light-doped LCMO.[17,19,24] Thus, we infer that the CAF state of bulk LCMO(0.005) is hindered by the anisotropic strain imposed from the NGO(001) substrate. Third, the LCMO film with $x = 0.429$ shows much weaker magnetism in the $M$–$T$ curve and higher resistivity in the $\rho$–$T$ curve. To further study the magnetism of the LCMO(0.429) film, we measured the $M$–$T$ curve in both field-cooling and field-warming processes for the LCMO(0.429) film [Fig. 3(c)]. A modest $T_C$ at 256 K and large thermal hysteresis observed in the $M$–$T$ curves indicate that the LCMO(0.429) film is phase separated (PS). Namely, antiferromagnetic insulating (AFI) phase and FM phase coexist and compete with each other at microscopic scale.[25] Combining with the overall magnetization and conductivity, we can conclude that the PS in the LCMO(0.429) film is AFI-dominated, similar to the heavy-doped LCMO bulk compounds ($x \sim 0.5$).[26–28] In summary, the 35 nm-thick LCMO/NGO(001) films with $0.005 < x < 0.429$ show a phase diagram similar to the bulk compounds. However, the LCMO(0.005) and LCMO(0.429) films show ground states similar to the bulk compositions with higher $x$. The anisotropic strain provided by the NGO (001) substrate could be responsible for such a deviation of ground states.

We next investigate the magnetic and electrical properties of the LCMO($x$)/SRO SLs. As shown in Fig. 3(d), the $M$–$T$ curves of LCMO($x$)/SRO SLs differ from those of the bulk compounds. And the corresponding MIT observed in the $\rho$–$T$ [Fig. 3(e)] are smeared due to the highly conductive SRO layers.[29,30] For the first set ($x = 0.200$, 0.250, and 0.333), the SLs show clear ferromagnetic transitions. Compared to the bulk counterparts, the $T_C$ are considerably enhanced by 99 K, 74 K, and 42 K, respectively. For the second set ($x = 0.005$ and 0.125), the $T_C$ are significantly enhanced by 94 K and 121 K, respectively. And the SLs also show clear drops of $M$ at 192 K for $x = 0.005$ and 160 K for $x = 0.125$, which can be attributed to the aforementioned CO-AF cluster state. Namely, the ferromagnetism of the LCMO layers in this set ($x = 0.005$ and 0.125) of SLs is also largely enhanced. Meanwhile, the CO-AF cluster state still exists and emerges at a higher $T$ than that in the LCMO/NGO(001) films. For the third set ($x = 0.429$), the $M$–$T$ curve of the SL is quite different from that of the LCMO/NGO(001) film. The SL first shows a moderate $T_C$ of 270 K, followed by a ferromagnetic transition with a small $M$ of $\sim 0.18$ $\mu_B$/Mn. Further decreasing $T$ down to 73 K, another ferromagnetic transition occurs with a rapid increment of $M$. We measured the $M$–$H$ curves at various $T$ to further probe the magnetism in the LCMO(0.429)/SRO SL. As shown in Fig. 3(f), the SL shows a quite slim $M$–$H$ hysteresis loop with small saturated magnetization ($M_s$) at 240 K (below the $T_C$) but square-shaped loops with high $M_s$ at 50 K and 15 K. We suggest that the LCMO(0.429) layer in the SL still shows a PS state below 270 K. At 240 K this layer shows CO-AF-dominated PS state, similar to the LCMO(0.429)/NGO(001) film. And the weak magnetic signal originates from the FM clusters embedded in the CO-AF background. Below 73 K, the LCMO/SRO interface effect may facilitate the FM state and destabilize the CO-AF state, leading to a strong FM signal.[31,32] Note that these ultrathin SRO layers are non-magnetic in the SLs, which is due to the dead layer effect.[30,33]

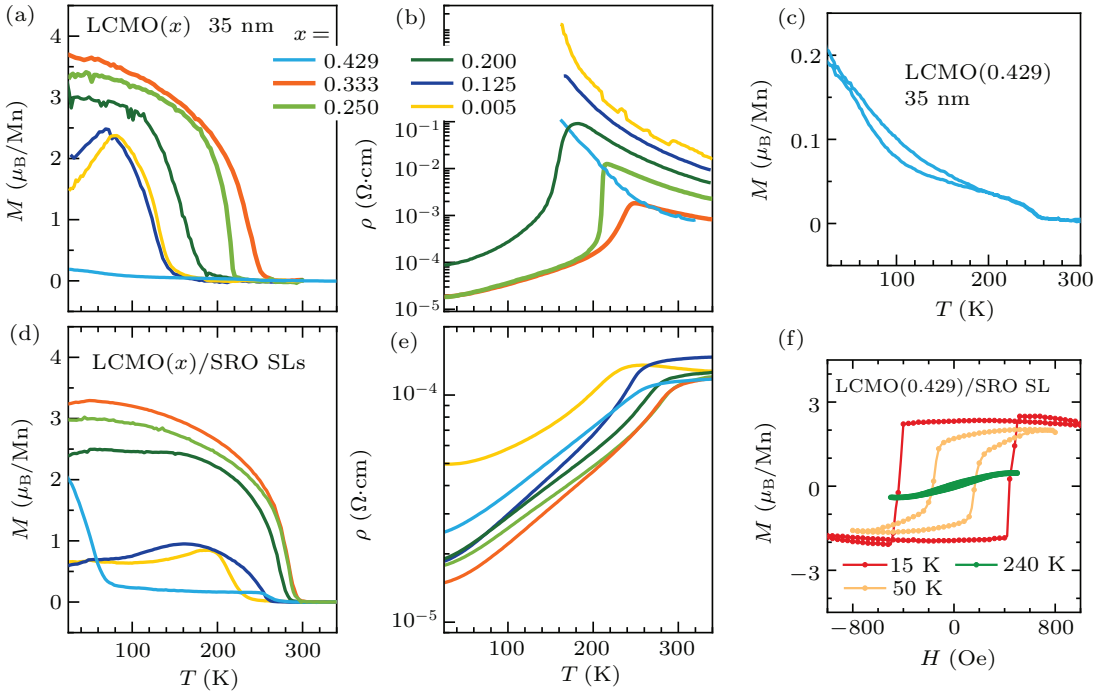



**Fig. 3.** Magnetic and electrical properties of 35 nm-thick LCMO($x$) single layers and LCMO($x$)/SRO SLs. The $M$–$T$ curves measured from (a) the single layers with a field of 500 Oe and (d) SLs with a field of 50 Oe applied along [010] axis. The paramagnetic signal from the NGO substrate has been subtracted. The $\rho$–$T$ curves measured from (b) the single layers and (e) SLs. (c) The $M$–$T$ curve of LCMO(0.429) single layer, measured from both cooling and warming processes with a field of 50 Oe applied. (f) The $M$–$H$ loops measured from the LCMO(0.429)/SRO SL.

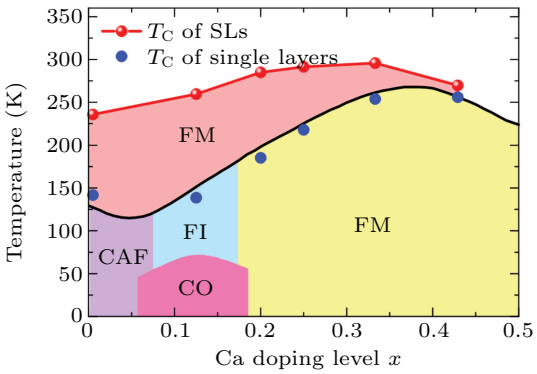



**Fig. 4.** The extended phase diagram together with the original phase diagram of LCMO($x$). The colored area under the black solid line shows the phase diagram of bulk LCMO($x$). The blue scatters represent the $T_C$ of 35 nm-thick LCMO($x$) single layers. The red scatters show the $T_C$ of LCMO($x$)/SRO SLs.

Based on the aforementioned electronic and magnetic characterizations, we obtained an extended phase diagram of LCMO($x$) by interfacial engineering (Fig. 4). Over the entire Ca doping range, the ferromagnetism in ultrathin LCMO($x$)/SRO SLs is improved. The corresponding enhancements in $T_C$ become larger in the lower doping level. In LCMO($x$), the ferromagnetism mainly originates from the DE interactions between $Mn^{3+}$ and $Mn^{4+}$, which is intimately correlated with the $e_g$ electron density and single-electron bandwidth ($W$) of the $e_g$ band.[34] The carrier density depends on the doping level of Ca and interfacial charge transfer. The $W$ is related to the Mn–O–Mn bond angle ($\Theta$) and the Mn–O bond length ($d$), given by the equation[35]

$$W \propto \cos\Theta / d^{3.5}. \quad (1)$$

Therefore, the enhanced ferromagnetism in LCMO($x$)/SRO SLs could originate from either the interfacial charge transfer or structural proximity effect, which will be separately discussed in the following part.

In the SLs, the SRO layers consist of $Ru^{4+}$ cations, while the LCMO layers consist of mixed $Mn^{3+}$ and $Mn^{4+}$. Therefore, the interfacial charge transfer is likely to change the $Mn^{3+}/Mn^{4+}$ ratio and the strength of the DE effect in the LCMO($x$) layers. Given the universal octahedral connectivity, the direction and magnitude of charge transfer at the $ABO_3/AB'O_3$ heterointerface highly depend on the energy levels of oxygen 2p bands ($\varepsilon_p$), with respect to their Fermi level ($E_F$).[6] The amount of transferred charge $\Delta n$ is proportional to the differences in $\varepsilon_p$ ($\Delta\varepsilon_p$) of $ABO_3$ and $AB'O_3$. The reference data of $\varepsilon_p$ for bulk SRO, $LaMnO_3$ (LMO), and $CaMnO_3$ (CMO) is $-3.40$ eV, $-3.57$ eV, and $-2.30$ eV, respectively.[6] The value of $\varepsilon_p$ for LCMO($x$) can be approximatively calculated from the linear interpolation

$$\varepsilon_p(\mathrm{LCMO}(x)) = \varepsilon_p(\mathrm{LMO}) \cdot (1-x) + \varepsilon_p(\mathrm{CMO}) \cdot x. \quad (2)$$

The calculated $\varepsilon_p$ of LCMO($x$) varies from $-3.56$ eV to $-3.03$ eV as Ca doping level $x$ increases from 0.005 to 0.429. Theoretically, the LCMO layers with $x = 0.005$ and 0.125 could dope electrons to SRO, while the SRO layer can dope electrons to LCMO layers with $x = 0.200$, 0.250, 0.333, 0.429. Following the charge transfer scenario, only the electron-doping into LCMO($x$) layers can stabilize the DE effect and improve the $T_C$. However, we experimentally observed $T_C$ enhancement in SLs with LCMO ($x = 0.005$ and

0.125) layers too. Accordingly, the charge transfer should not be the only driving force of the enhanced ferromagnetism in LCMO($x$)/SRO SLs.

Now we turn to explore the structural origin of the enhanced ferromagnetism. The structural proximity effect is another common origin of interfacial magnetic evolution. The interfacial OOC can modulate the octahedral tilt and rotation and therefore induce emergent properties in the oxides [schematically shown in Fig. 5(a)].[20] RSMs around NGO (116) and NGO ($\overline{1}16$) reflections were measured from the LCMO($x$)/SRO SLs. The RSMs results are shown in Figs. 5(b)–5(g), and the superlattice Bragg peaks (SLBPs) are labelled with red arrows. The asymmetry of the SLBPs position in (116) and ($\overline{1}16$) reflections manifests the octahedral tilting distortion, from which we can derive the tilt angle ($\delta$) and the B–O–B bond angle ($\Theta$).[21,36] The calculated $\Theta$ in the SLs and the corresponding bulk values are summarized in Fig. 5(h). The LCMO($x$)/SRO SLs exhibit much larger $\Theta$ than the bulk LCMO($x$), implying a clear suppression of octahedral tilt and rotation due to interfacial OOC. The increased $\Theta$ enlarges the $W$ of the LCMO($x$) layers in the SLs, therefore stabilizing the DE interaction and facilitating the ferromagnetism in the LCMO($x$) layers.

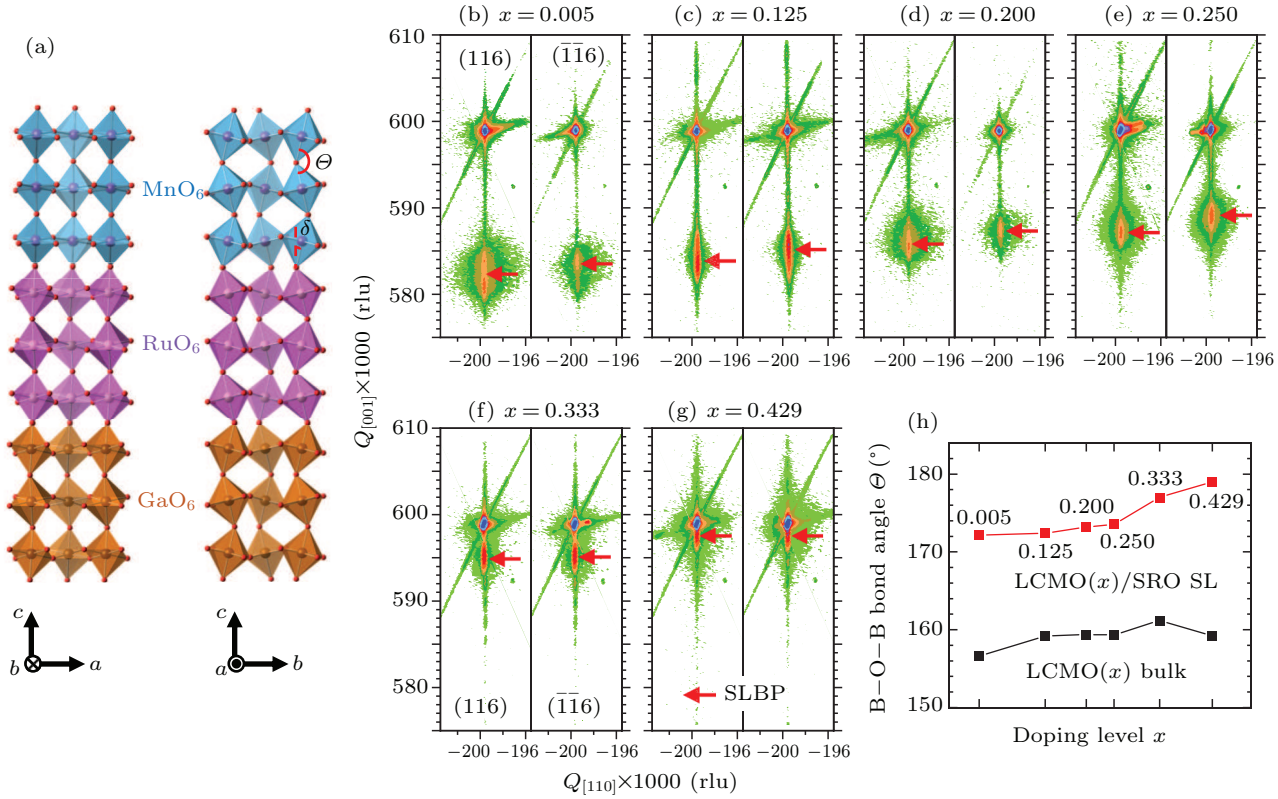



**Fig. 5.** (a) Schematics of the octahedral connectivity across the LCMO/SRO/NGO (001) interfaces viewed along the $b$-axis and $a$-axis. (b)–(g) RSMs measured around NGO (116) and NGO ($\overline{1}16$) reflections from the LCMO($x$)/SRO SLs. The SLBP in each figure is marked by the red arrow. (h) The B-O-B bond angle of the LCMO($x$)/SRO SLs derived from RSMs. The Mn–O–Mn bond angles of bulk LCMO($x$) are also shown for comparison.

At last, we would like to discuss the $T_C$ enhancements in two special cases: the SLs with light doped ($x = 0.005$, 0.125) and heavy doped ($x = 0.429$) LCMO. In light doped LCMO($x$), the $Mn^{3+}$–$Mn^{3+}$ SE interaction dominates over the $Mn^{3+}$–$Mn^{4+}$ DE interaction, favoring CO or AF states and destabilizing the FM state.[24,37] In the LCMO/SRO SLs with $x = 0.005$, 0.125, the enhanced B–O–B bond angle can not only enhance the DE interaction but also suppress the SE interaction. As a consequence, the interface-induced $T_C$ enhancements for the light-doped cases become much more pronounced than the SLs with higher $x$. For the SLs with heavy-doped ($x = 0.429$) LCMO, on the contrary, the $T_C$ enhancement is rather small. And the small $M_s$ signifies a PS state with large amount of CO-AF phase. Note that reducing $T$ always destabilizes the CO-AF phase and facilitates the FM phase in the PS state.[38] Therefore, we also observed a re-entry of FM phase at 73 K, which also originates from the interface-enhanced DE interaction.

## 4. Conclusion

In summary, we systematically investigated the distinct magnetic and electrical properties of epitaxial LCMO($x$) single layers and LCMO($x$)/SRO SLs. For all the Ca doping levels, the $T_C$ in LCMO($x$)/SRO SLs are significantly improved from the corresponding bulk and single LCMO layers with interfacial engineering. Also, we found a pronounced increase of B–O–B bond angle in the LCMO($x$)/SRO SLs, which should be the main driving force of the enhanced

ferromagnetism. Accordingly, we constructed an extended phase diagram of LCMO($x$) with interfacial engineering. Our work paves a way to stabilize the ferromagnetism in ultrathin LCMO($x$) films covering a wide doping range, holding abundant application potentials for oxide-based electronic devices.

## References


[1] Chakhalian J, Freeland J W, Millis A J, Panagopoulos C and Rondinelli J M 2014 *Rev. Mod. Phys.* **86** 1189

[2] Hwang H Y, Iwasa Y, Kawasaki M, Keimer B, Nagaosa N and Tokura Y 2012 *Nat. Mater.* **11** 103

[3] Rondinelli J M and Spaldin N A 2011 *Adv. Mater.* **23** 3363

[4] Gao, Y.; Wang J, Wu L, Bao S, Shen Y, Lin Y and Nan C 2015 *Sci. China Mater.* **58** 302

[5] Moon E J, Balachandran P V, Kirby B J, Keavney D J, Sichel-Tissot R J, Schleputz C M, Karapetrova E, Cheng X M, Rondinelli J M and May S J 2014 *Nano. Lett.* **14** 2509

[6] Zhong Z and Hansmann P 2017 *Phys. Rev. X* **7** 011023

[7] Grisolia M N, Varignon J, Sanchez-Santolino G, Arora A, Valencia S, Varela M, Abrudan R, Weschke E, Schierle E, Rault J E, Rueff J P, Barthelemy A, Santamaria J and Bibes M 2016 *Nat. Phys.* **12** 484

[8] Chen H and Millis A 2017 *J. Phys. Condens. Matter.* **29** 243001

[9] Hoffman J, Tung I C, Nelson-Cheeseman B B, Liu M, Freeland J W and Bhattacharya A 2013 *Phys. Rev. B* **88** 144411

[10] Shiomi Y, Handa Y, Kikkawa T and Saitoh E 2015 *Phys. Rev. B* **92** 024418

[11] Ziese M, Bern F, Pippel E, Hesse D and Vrejoiu I 2012 *Nano Lett.* **12** 4276

[12] He C, Grutter A J, Gu M, Browning N D, Takamura Y, Kirby B J, Borchers J A, Kim J W, Fitzsimmons M R, Zhai X, Mehta V V, Wong F J and Suzuki Y 2012 *Phys. Rev. Lett.* **109** 197202

[13] Chen B B, Chen P F, Xu H R, Jin F, Guo Z, Lan D, Wan S Y, Gao G Y, Chen F and Wu W B 2016 *ACS Appl. Mater. Interfaces* **8** 34924

[14] Chen B B, Chen P F, Xu H R, Tan X L, Jin F, Guo Z, Zhi B W and Wu W B 2014 *Appl. Phys. Lett.* **104** 242416

[15] Chen P F, Chen B B, Tan X L, Xu H R, Xuan X F, Guo Z, Jin F and Wu W B 2013 *Appl. Phys. Lett.* **103** 262402

[16] Lan D, Chen B B, Qu L L, Jin F, Guo Z, Xu L Q, Zhang K X, Gao G Y, Chen F, Jin S W, Wang L F and Wu W B 2019 *ACS Appl. Mater. Interfaces* **11** 10399

[17] Dagotto E, Hotta T and Moreo A 2001 *Phys. Rep.* **344** 1

[18] Yunoki S, Hotta T and Dagotto E 2000 *Phys. Rev. Lett.* **84** 3714

[19] Gennes P G 1960 *Phys. Rev.* **118** 141

[20] Huijben M, Koster G, Liao Z L and Rijnders G 2017 *Appl. Phys. Rev.* **4** 041103

[21] Tan X L, Gao G Y, Chen P F, Xu H R, Zhi B W, Jin F, Chen F and Wu W B 2014 *J. Appl. Phys.* **116** 203706

[22] Dai P C, Fernandez-Baca J A, Wakabayashi N, Plummer E W, Tomioka Y and Tokura Y 2000 *Phys. Rev. Lett.* **85** 2553

[23] Likodimos V and Pissas M 2006 *Phys. Rev. B* **73** 214417

[24] Bose E, Karmakar S, Chaudhuri B K and Pal S 2008 *Solid State Commun.* **145** 149

[25] Wang L F, Tan X L, Chen P F, Zhi B W, Sun Z G, Huang Z, Gao G Y and Wu W B 2013 *Appl. Phys. Lett.* **103** 072407

[26] Tao J, Niebieskikwiat D, Varela M, Luo W, Schofield M A, Zhu Y, Salamon M B, Zuo J M, Pantelides S T and Pennycook S J 2009 *Phys. Rev. Lett.* **103** 097202

[27] Radaelli P. G, Cox D E, Marezio M and Cheong S W 1997 *Phys. Rev. B* **55** 3015

[28] Huang Q, Lynn J W, Erwin R W, Santoro A, Dender D C, Smolyaninova V N, Ghosh K and Greene R L 2000 *Phys. Rev. B* **61** 8895

[29] Cao G, McCall S, Shepard M and Crow J E 1997 *Phys. Rev. B* **56** 321

[30] Chang Y J, Kim C H, Phark S H, Kim Y S, Yu J and Noh T W 2009 *Phys. Rev. Lett.* **103** 057201

[31] Huang Z, Wang L F, Tan X L, Chen P F, Gao G Y and Wu W B 2010 *J. Appl. Phys.* **108** 083912

[32] Zhang H R, Liu Y B, Wang S H, Hong D S, Wu W B and Sun J R 2016 *Chin. Phys. B* **25** 077306

[33] Chang S H, Chang Y J, Jang S Y., Jeong D W, Jung C U, Kim Y J, Chung J S and Noh T W 2011 *Phys. Rev. B* **84** 104101

[34] Masrour R and Jabar A 2016 *Chin. Phys. B* **25** 107502

[35] Berndt L M, Balbarin V and Suzuki Y 2000 *Appl. Phys. Lett.* **77** 2903

[36] Gao G Y, Yin Z Z, Huang Z, Jin S W and Wu W B 2008 *J. Phys. D: Appl. Phys.* **41** 152001

[37] Algarabel P A, De Teresa J M, Blasco J, Ibarra M R, Kapusta C, Sikora M, Zajac D, Riedi P C and Ritter C 2003 *Phys. Rev. B* **67** 134402

[38] Huang Z, Wang L F, Chen P F, Gao G Y, Tan X L, Zhi B W, Xuan X F and Wu W B 2012 *Phys. Rev. B* **86** 014410